The Astrophysical Journal Letters, 1009:L24 (11pp), 2026 October 1 https://doi.org/10.3847/2041-8213/aea295
© 2026. The Author(s). Published by the American Astronomical Society.
OPEN ACCESS

Spectroscopic Signatures of Nonuniform Lateral Expansion of a Coronal Mass Ejection in the Low Corona with ADITYA-L1/VELC

Saurabh Tripathi[1,2], Tanmoy Samanta[1,2], and Jayant Joshi[1,2]
[1] Indian Institute of Astrophysics, Koramangala, Bangalore, 560034, India; tanmoy.samanta@iiap.res.in
[2] Pondicherry University, 605014, Puducherry, India
Received 2026 August 24; accepted 2026 September 4; published 2026 September 25

Abstract

Coronal mass ejections (CMEs) undergo rapid evolution in the low corona ($<2R_{\odot}$), yet their three-dimensional kinematics remain poorly constrained. We present a spectroscopic and imaging analysis of a CME observed on 2024 August 5 using the Visible Emission Line Coronagraph (VELC) on board ADITYA-L1 and Atmospheric Imaging Assembly (AIA)/Solar Dynamics Observator (SDO). The VELC Fe XIV 5303 Å spectra captured the erupting CME as it crossed the western slit. Space-time maps from single-Gaussian fits reveal coronal dimming and enhanced Doppler velocities during the eruption. Detailed spectral analysis reveals strongly Doppler-shifted secondary components associated with the CME front. These components appear as two spatially separated emission branches on opposite sides of the rest wavelength, producing a distinct bifurcated spectral morphology superposed on the nearly stationary reduced-intensity coronal emission. Double-Gaussian fitting yields line-of-sight (LOS) plasma velocities of up to 218 km s^{-1}, likely a lower limit as the secondary component reaches the edge of spectral window. AIA 211 Å observations measure a projected radial speed of 1135 km s^{-1}, larger than the plane-of-sky (POS) lateral speed of 692 km s^{-1} along the slit. To interpret the observed CME evolution and spectral structure, we developed a simplified three-dimensional geometric-kinematic model of an expanding axially tilted CME shell. Synthetic spectra from the model show that an inclined CME undergoing asymmetric lateral expansion can produce a bifurcated spectral morphology similar to that observed, with velocity components projected in the radial, POS-lateral, and LOS-lateral directions. Our results demonstrate that combining spectroscopy and EUV imaging constrains different components of CME kinematics during early evolution.

Unified Astronomy Thesaurus concepts: Solar coronal mass ejections (310); Solar corona (1483); Spectroscopy (1558); Active sun (18); Solar flares (1496); Solar activity (1475); Solar storm (1526); Doppler shift (401); The Sun (1693)

Materials only available in the online version of record: animations

1. Introduction

Coronal mass ejections (CMEs) are large-scale eruptions of magnetized plasma, often associated with solar flares and the release of coronal magnetic energy (J. T. Gosling et al. 1990; K. Shibata & T. Magara 2011; D. F. Webb & T. A. Howard 2012; J. Chen 2017; M. K. Georgoulis et al. 2019). Their initial acceleration and structural evolution in the low corona influence their subsequent propagation in the heliosphere (N. Gopalswamy 2004; P. F. Chen 2011; A. Vourlidas 2021; R. A. Howard et al. 2023). However, observations of this early phase remain limited because coronagraphs have limited coverage of the low corona.

White-light observations from Large Angle and Spectrometric Coronagraph (LASCO) coronagraph on board the Solar and Heliospheric Observatory (SOHO) and COR2 coronagraph on board STEREO mainly track CME structures above about 2 $R_{\odot}$ (G. E. Brueckner et al. 1995; R. A. Howard et al. 2008; D. F. Webb & T. A. Howard 2012). Multiviewpoint observations have enabled reconstruction of the three-dimensional CME morphology and propagation direction using geometric models such as the Graduated Cylindrical Shell (GCS) model (A. F. R. Thernisien et al. 2006; A. Thernisien et al. 2009; A. Thernisien 2011). These observations have also shown that CME expansion can differ between the radial and lateral directions (S. Majumdar et al. 2020; A. Agarwal et al. 2026).

The early evolution of CMEs in the low corona is primarily observed using EUV imagers, such as Extreme ultraviolet Imaging Telescope (EIT) on board SOHO and Atmospheric Imaging Assembly (AIA) (J. R. Lemen et al. 2012) on board the Solar Dynamics Observatory (SDO), which capture the plane-of-sky (POS) evolution of erupting structures and associated phenomena such as EUV waves and coronal dimmings (N. Gopalswamy & Y. Hanaoka 1998; D. M. Zarro et al. 1999; S. W. McIntosh et al. 2010; S. Patsourakos et al. 2010; K. A. Kozarev et al. 2011, 2017; S. Ma et al. 2011; X. Cheng et al. 2012; W. Liu et al. 2012; S. Patsourakos & A. Vourlidas 2012; W. Liu & L. Ofman 2014; A. Warmuth 2015; F. Frassati et al. 2020; A. M. Veronig et al. 2025). Spectroscopic observations from Ultraviolet Coronagraph Spectrometer (UVCS) on board SOHO (J. L. Kohl et al. 1995) and EUV Imaging Spectrometer (EIS) on board Hinode (J. L. Culhane et al. 2007) have shown that CMEs contain multiple plasma components with different line-of-sight (LOS) velocities (J. C. Raymond et al. 2000; E. Landi et al. 2010; H. Tian et al. 2012). UVCS observations of fast flare-associated CMEs have revealed large Doppler shifts associated with rapid expansion and high-temperature plasma during eruptions (J. C. Raymond et al. 2003). Such observations provide

Original content from this work may be used under the terms of the Creative Commons Attribution 4.0 licence. Any further distribution of this work must maintain attribution to the author(s) and the title of the work, journal citation and DOI.

information on CME motions along the line of sight that cannot be obtained from imaging alone. Ground-based spectroscopic observations and forward-modeling studies have further demonstrated the potential of coronal emission-line spectroscopy to constrain the kinematics, thermodynamic properties, and magnetic structure of CMEs in the low corona (H. Tian et al. 2013; X. Liu et al. 2023; L. Chan et al. 2025; E. M. Wraback et al. 2025).

The Visible Emission Line Coronagraph (VELC) on board ADITYA-L1 (J. Singh et al. 2019; M. Priyal et al. 2024; R. Ramesh et al. 2024; V. Muthu Priyal et al. 2025; V. M. Priyal et al. 2025; J. Singh et al. 2025) provides spectroscopic observations of the low corona. Its multislit design enables high-cadence observations of the Fe XIV 5303 Å green line, which traces hot (∼1.8 MK) coronal plasma at heights of 1.05–1.5 $R_{\odot}$, where the early evolution of CMEs can be studied spectroscopically.

In this Letter, we investigate the early evolution of a fast CME observed on 2024 August 5 using Fe XIV 5303 Å spectroscopy from VELC together with AIA observations. We use the VELC spectra to examine the Doppler-shifted emission associated with the erupting plasma and combine these measurements with the POS evolution seen in EUV images. In particular, we investigate whether the lateral expansion of the CME is uniform in different directions and how its LOS velocity structure is related to the observed POS evolution. We further use a simplified three-dimensional model to examine how the CME orientation and nonuniform lateral expansion contribute to the observed spectral structure.

2. Observations and Data Reduction

On 2024 August 5, active region NOAA 13767 produced an X1.7-class flare at approximately 13:27 UT near the west limb (97°W, 8°S), followed by a fast CME. The CME was observed by VELC on board ADITYA-L1, together with AIA. During this period, the VELC spectrograph operated in a sit-and-stare mode. Slit S4 was positioned near the western limb at Solar $X \approx 1080''$ and captured the CME as it propagated through the VELC field of view (Figure 1). The Fe XIV 5303 Å observations have a cadence of 51 s and a spatial sampling of $2\farcs5$ pixel^{-1} along the slit (corresponding to 2 pixel on-board binning), and a spectral sampling of 0.028 Å pixel^{-1}. Each slit has a width of $9\farcs6$. We use AIA 211 Å images, sensitive to plasma at approximately 2 MK, with a spatial sampling of $0\farcs6$ pixel^{-1} and a cadence of 12 s. A routine VELC raster scan obtained approximately 13 hr before the eruption provides the preeruption coronal context (Figure 1).

We use Level-1 Fe XIV 5303 Å spectroscopic data obtained from the Indian Space Science Data Centre (ISSDC; M. Priyal et al. 2024; J. Singh et al. 2025). The data were first corrected for dark current and detector bias. Since dedicated in-flight flat-field observations are not available, flat-field and prefilter corrections were derived for each slit by averaging VELC raster observations obtained between 2024 July and September. Wavelength calibration was performed using photospheric absorption lines from solar disk light scattered off the primary mirror, assuming zero Doppler shift for these lines. Spectral curvature along the slit was also corrected. The photospheric contribution was removed using three-month averaged observations. Small temporal variations in the photospheric absorption-line depths leave residuals in the processed spectra. To minimize their influence, regions spanning approximately 10 pixels around the centers of the two strong absorption lines were not included in the spectral fitting. These masked regions are shown by the gray shaded areas in Figures 2(d) and 3(c)–(d). The resulting coronal Fe XIV emission profiles were fitted with a single Gaussian to obtain the peak intensity, Doppler velocity, and line width, using a rest wavelength of 5302.8 Å (Figures 1(e)–(g)). Finally, small spatial shifts along the slit caused by satellite drift were corrected using a cross-correlation technique. Drift perpendicular to the slit cannot be corrected and causes slow intensity variations with time in the space-time maps, as the slit samples slightly different coronal regions during the observing sequence. Some of the gradual brightening and fading patterns seen in the intensity maps may therefore arise from this effect (see Figure 1(e)).

3. Results

3.1. CME Evolution in AIA and VELC Observations

Figures 1(d)–(g) shows the evolution of the CME along Slit S4 from 12:42 to 14:03 UT. The AIA 211 Å space-time map (Figure 1(d)) shows the onset of the eruption at around 13:27 UT, followed by an outward-propagating bright front and a pronounced intensity depletion between Solar $Y \approx -450''$ and $50''$. The corresponding decrease in VELC Fe XIV 5303 Å intensity (Figure 1(e)) indicates depletion of coronal emission along the slit. As the CME expands, enhanced emission develops near the propagating front, while depletion and redistribution of coronal plasma occur in its wake, producing the associated coronal dimming. The Doppler map shows red- and blueshifted emission during the CME passage (Figure 1(f)). The Fe XIV line width also increases during the passage of the CME front, with FWHM values exceeding 1.5 Å (Figure 1(g)).

Figure 2 provides a closer view of the CME evolution along Slit S4 between 13:27 and 13:30 UT. The AIA 211 Å base-difference images in Figure 2(a) show the outward propagation of the CME-associated front and the progressive development of the dimming region. The corresponding VELC Fe XIV 5303 Å spectral maps in Figure 2(b) show the evolution of the emission simultaneously in the wavelength–height plane. At the beginning of the sequence, the emission is concentrated close to the Fe XIV rest wavelength. As the CME front crosses the slit, enhanced emission develops over an extended range of Solar Y and wavelength, and the spectral structure changes with time as the CME propagates.

The CME-associated spectral changes are more clearly seen in the base-difference maps shown in Figure 2(c). A pronounced reduction in the spectral intensity relative to the preeruption state is seen during the CME passage, particularly around the strong coronal emission near the Fe XIV 5303 Å line. Superposed on this depletion, transient emission extends into both the red and blue wings. Around 13:27:57 UT, the wing emission develops into two distinct branches on opposite sides of the Fe XIV rest wavelength. The branches are also separated along the Solar Y direction, with the redshifted emission predominantly appearing at lower heights and the blueshifted emission at higher heights. They have different spectral extents, and their positions and shapes evolve as the CME propagates. The evolving red- and blueshifted branches, highlighted by the yellow dotted curves in Figure 2(c), form the characteristic two-branch spectral structure. We refer to this evolving structure as the bifurcated spectral morphology.

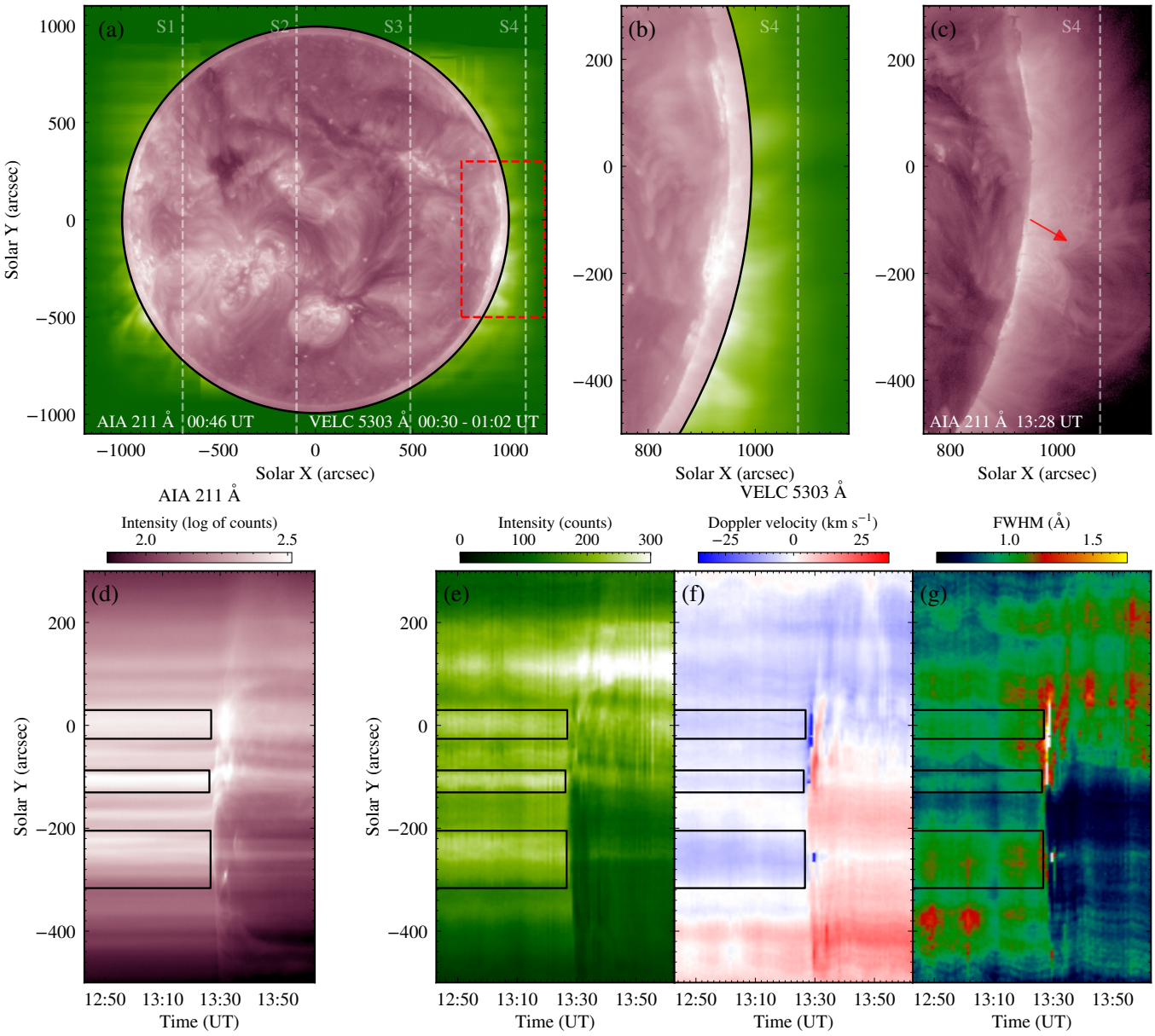


Figure 1. VELC and AIA observations of the CME observed on 2024 August 5 and its space-time evolution at VELC slit S4. (a) Full-disk composite image before the eruption: the VELC Fe XIV 5303 Å raster covering 1.05–1.30 $R_\odot$ and the spatially binned AIA 211 Å image covering 0–1.05 $R_\odot$. The four VELC slit positions are overlaid and the red dashed box marks the western-limb region. (b) Expanded view of this region. (c) AIA 211 Å image during the CME eruption, with VELC Slit S4 (Solar $X \approx 1080''$) marked. (d)–(g) Space-time maps along Slit S4 from 12:42 to 14:03 UT. (d) AIA 211 Å intensity; (e) VELC Fe XIV 5303 Å peak intensity; (f) Doppler velocity; and (g) line width (FWHM), all derived from a single-Gaussian fit to the VELC spectra. Examples of the Gaussian fits are shown in Figure 2. Three black rectangular boxes highlight the prominent preeruption features in the VELC intensity space-time map (panel (e)) and are overlaid on panels (d)–(g) for easier comparison.

The one-dimensional profiles extracted at selected locations within these structures (Figure 2(d)) provide a closer view of the spectral features seen in Figure 2(c). The profiles were spatially averaged over three adjacent slit pixels and smoothed using a three-point running average in wavelength before fitting. The selected profiles show additional wing emission compared with the preeruption profiles, with its direction and extent varying with Solar *Y*. The single-Gaussian fits reproduce the main coronal emission near the line center but leave systematic residuals in the wings (Figure 2(e)), indicating additional spectral components associated with the CME. We therefore examine these kinds of profiles using multicomponent Gaussian fitting in the following section.

3.2. Multicomponent Spectral Fitting

Figure 3 shows the Fe XIV 5303 Å profiles at two representative locations along Slit S4 during the CME passage (13:28:48 UT), together with the corresponding preeruption profiles. Each profile was fitted with a linear background, a primary Gaussian component representing the ambient coronal

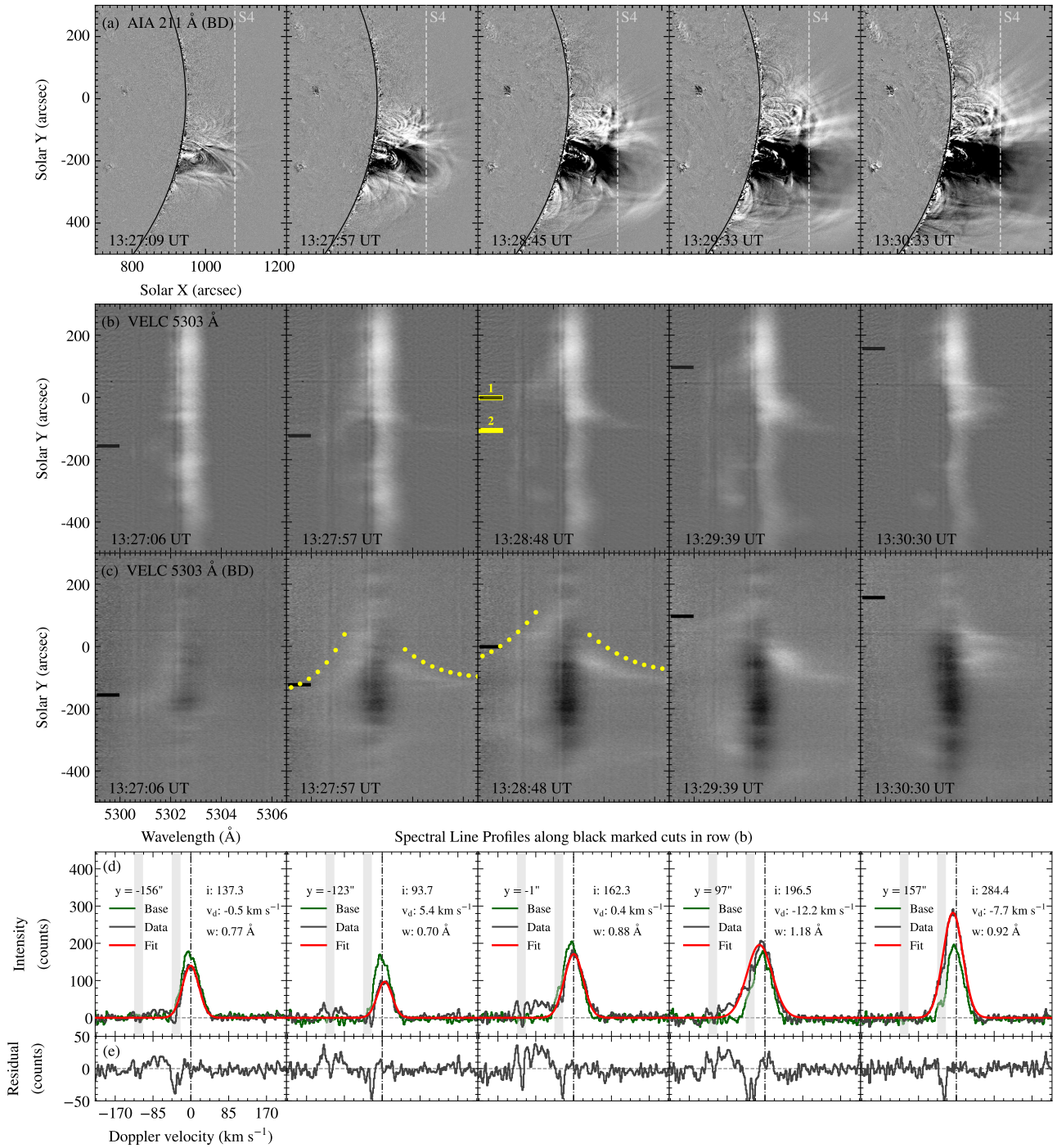


Figure 2. Imaging and spectroscopic evolution of the CME along VELC Slit S4 from 13:27 to 13:30 UT. (a) AIA 211 Å base-difference images showing the propagating CME front and the developing coronal dimming. (b) VELC Fe XIV 5303 Å spectral maps along Slit S4, showing the emission as a function of wavelength and solar Y. (c) Corresponding base-difference spectral maps, which more clearly highlight the CME-associated intensity depletion near the Fe XIV rest wavelength and the bifurcated red- and blueshifted structures highlighted by the yellow dotted lines. (d) Representative spectra extracted at the spatial locations marked by the black lines in panel (b), showing the observed profiles (dark gray), preevent reference profiles (green), and single-Gaussian fits to the observed profiles (red). The fitted intensity (i), Doppler velocity (v_d), and FWHM (w) are also shown. The shaded wavelength regions are excluded from the fits. (e) Residuals of the single-Gaussian fits to the observed profiles. The profiles marked by the yellow line segments in panel (b) are used for the multi-Gaussian analysis in Figure 3. An animation showing the time evolution of panels (a)–(c) of this figure is available online.

(An animation of this figure is available in the online article.)

emission, and an additional Gaussian component to account for the Doppler-shifted CME-associated emission.

At Solar $Y \approx -1''$ (Figure 3(c)), the primary component has a Doppler velocity of $+2.6\,\mathrm{km\,s^{-1}}$ and FWHM of 0.84 Å while the secondary component is blueshifted by $-81.0\,\mathrm{km\,s^{-1}}$ with FWHM of 1.23 Å. At Solar $Y \approx -106''$ (Figure 3(d)), the primary component has $+5.8\,\mathrm{km\,s^{-1}}$ and FWHM of 0.70 Å while the secondary component is redshifted by $+217.9\,\mathrm{km\,s^{-1}}$ with FWHM of 0.80 Å. The primary components remain close to the rest wavelength, while the secondary components are

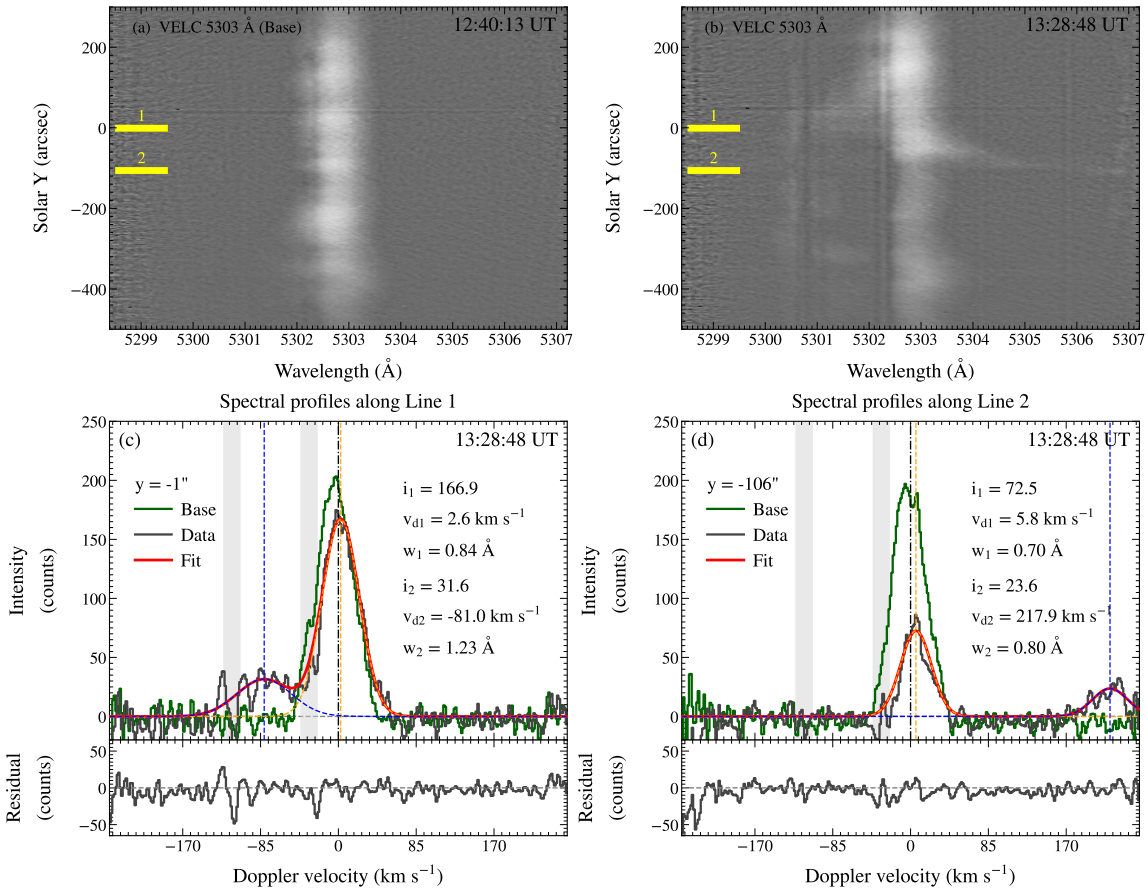


Figure 3. Multicomponent Gaussian analysis of the VELC Fe XIV 5303 Å spectra during the CME passage. (a) and (b) show spectra along Slit S4 at the preevent reference time (12:40:13 UT) and during the CME passage (13:28:48 UT), respectively. (c) and (d) present at Solar $Y = -1''$ and Solar $Y = -106''$, respectively, at the locations marked by the yellow line segments in panels (a) and (b). The observed profiles (dark gray) are compared with the preevent reference profiles (green). The double-Gaussian fits (red) consist of a primary core component (yellow) and a Doppler-shifted secondary component (blue). The fitted intensity, Doppler velocity, and FWHM are printed for each component, with subscripts 1 and 2 denoting the primary and secondary components, respectively. The shaded wavelength regions are excluded from the fits. The lower panels show the corresponding postfit residuals.

strongly Doppler shifted and have broader line widths. Their spatial separation is consistent with the two-branch structure identified in Figure 2.

3.3. Radial and Lateral Propagation

The LOS velocities of the erupting plasma were established from the spectral analysis above. We next examine the radial and lateral propagation of the CME using the complementary AIA and VELC observations. Figure 4 summarizes these measurements.

Figures 4(a)–(c) shows the radial propagation of the CME in the POS. An artificial slit at a position angle of 101.°5 was placed along the propagation direction (Figure 4(a)), and the CME leading edge was tracked in the corresponding space-time map (Figures 4(b)–(c)). A linear fit to the manually tracked bright propagating front gives a projected radial propagation speed of $1134.9 \pm 33.4\,\mathrm{km\,s^{-1}}$.

To examine the lateral evolution, we use the cospatial AIA and VELC observations along Slit S4. Tracking the propagating front in the AIA space-time map gives a projected POS propagation speed of $691.5 \pm 30.7\,\mathrm{km\,s^{-1}}$.

The VELC spectra further allow the propagation of emission features to be examined over selected Doppler-velocity ranges. We define three artificial slits (C1–C3) in the red wing of the Fe XIV profile, corresponding to Doppler velocities of +37, +93, and $+192\,\mathrm{km\,s^{-1}}$, respectively, to investigate the spatiotemporal evolution of the CME-associated emission. The red wing is used because these features have higher signal-to-noise ratios and more coherent ridges than the corresponding blue-wing features. The ridge positions were obtained by fitting the intensity profile at each height with a Gaussian, followed by linear fits to the resulting height–time tracks. Although a blueshifted component is clearly visible in the individual spectra, the corresponding blue-wing space-time features are too diffuse for a reliable propagation-speed measurement.

The three red-wing velocity ranges give projected POS propagation speeds of ∼602, 532, and $462\,\mathrm{km\,s^{-1}}$, respectively. The projected propagation speed therefore decreases as the redshifted velocity increases. This trend does not necessarily imply a decrease in the actual plasma speed, but can result from the changing direction of the expansion velocity across the CME shell. Since Slit S4 samples the expanding CME shell at a fixed location, different positions along the slit intersect different parts of the shell. Near the POS-lateral front of the expanding shell sampled along the slit, the expansion velocity is predominantly in the POS, giving a larger projected POS speed and a smaller LOS component. Toward the central part of the shell sampled by the slit, the expansion velocity has a larger LOS component, producing a larger Doppler shift and a smaller projected POS speed. The

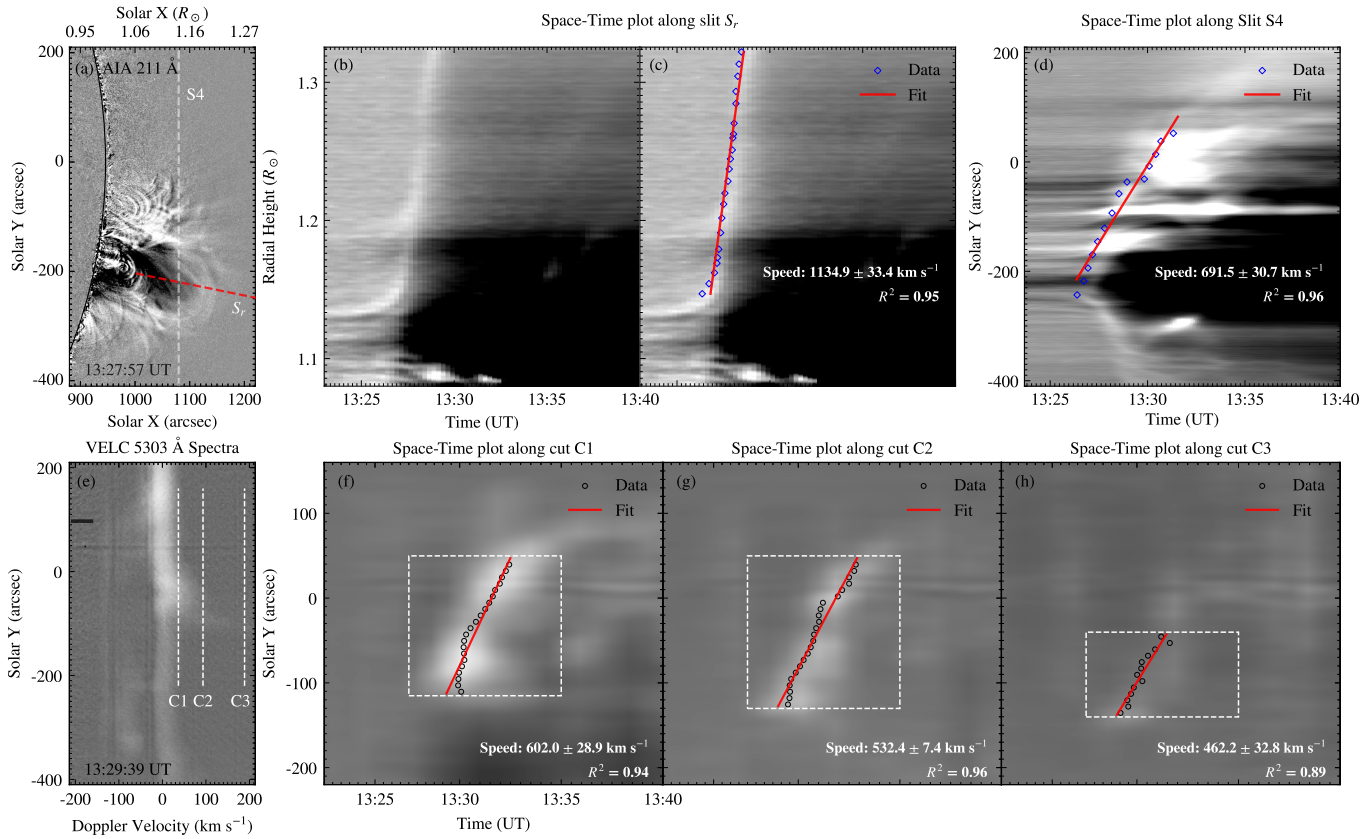


Figure 4. Radial and lateral propagation of the CME and Doppler-resolved propagation of VELC emission features. (a) AIA 211 Å image showing the artificial slit (red dashed line, S_r) placed along the CME radial propagation direction, together with VELC Slit S4 (white dashed line). (b) AIA 211 Å base-difference space-time map along the artificial slit S_r. (c) Same as (b), with the manually tracked CME propagating front (blue diamonds) and its linear fit (red line). (d) AIA 211 Å base-difference space-time map along VELC Slit S4, showing the manually tracked lateral front (blue diamonds) and its linear fit (red line). (e) VELC Fe XIV 5303 Å spectrum at 13:29:39 UT, with three artificial cuts (C1–C3) marked at Doppler velocities of 37, 93, and 192 km s^{-1}, respectively. (f)–(h) Space-time intensity maps constructed from the three cuts. For cuts C1 and C2, the emission is averaged over a ±14 km s^{-1} Doppler-shift range around their central velocities, while for cut C3 it is averaged over a ±28 km s^{-1} range. The positions of the emission peaks (black circles) are obtained from Gaussian fits to the intensity profiles at each height within the marked regions (white dashed rectangles), and the resulting tracks are fitted linearly (red lines) to determine the propagation speeds. The measured propagation speeds and corresponding R^2 values are indicated in the respective panels.

velocity-resolved propagation therefore indicates a systematic change in the direction of the expansion velocity across the observed CME shell.

This behavior is consistent with an expanding CME in which the lateral velocity has components both in the POS and along the LOS, as explored with the three-dimensional model in Section 3.4.

3.4. Three-dimensional Modeling of the CME

To investigate the geometric origin of the bifurcated VELC spectra, we use a parameterized three-dimensional kinematic model of an expanding CME. The model consists of a shell-like structure undergoing radial propagation and lateral expansion, with the lateral velocity specified independently along two perpendicular directions. The model geometry and velocity prescription are described in Appendix A.

We synthesize the Fe XIV 5303 Å emission by integrating the optically thin emission along the line of sight. The synthetic spectra are used only for a qualitative comparison with the VELC observations. The model parameters are representative and are not intended to provide a quantitative or unique reconstruction of the three-dimensional CME geometry or velocity field.

Figure 5 shows four representative configurations designed to separate the effects of CME orientation and lateral expansion. Case 1 represents a limb CME with symmetric lateral expansion, producing approximately symmetric red- and blueshifted components with a semicircular morphology. Case 2 introduces the heliographic location and axis tilt obtained from the GCS reconstruction (Appendix B) while retaining symmetric lateral expansion. The resulting projection produces unequal Doppler shifts. For Cases 1 and 2, the lateral cross-section is circular because the expansion is symmetric, so the axis tilt is not applicable. Case 3 retains the limb geometry but introduces asymmetric lateral expansion, with a larger expansion speed along the LOS than along the Solar Y direction. This changes the spectral shape, producing a more pointed morphology. Case 4 combines the GCS-constrained orientation, including axis tilt, with asymmetric lateral expansion and produces a spectral pattern most similar to that observed by VELC.

The comparison shows that the CME orientation, axis tilt and lateral expansion affect different aspects of the observed spectral structure. The axis tilt and orientation primarily determine the relative displacement and Doppler asymmetry of the red- and blueshifted components, respectively, whereas the distribution of lateral expansion controls their spectral extent and shape. The accompanying animation shows the synthetic

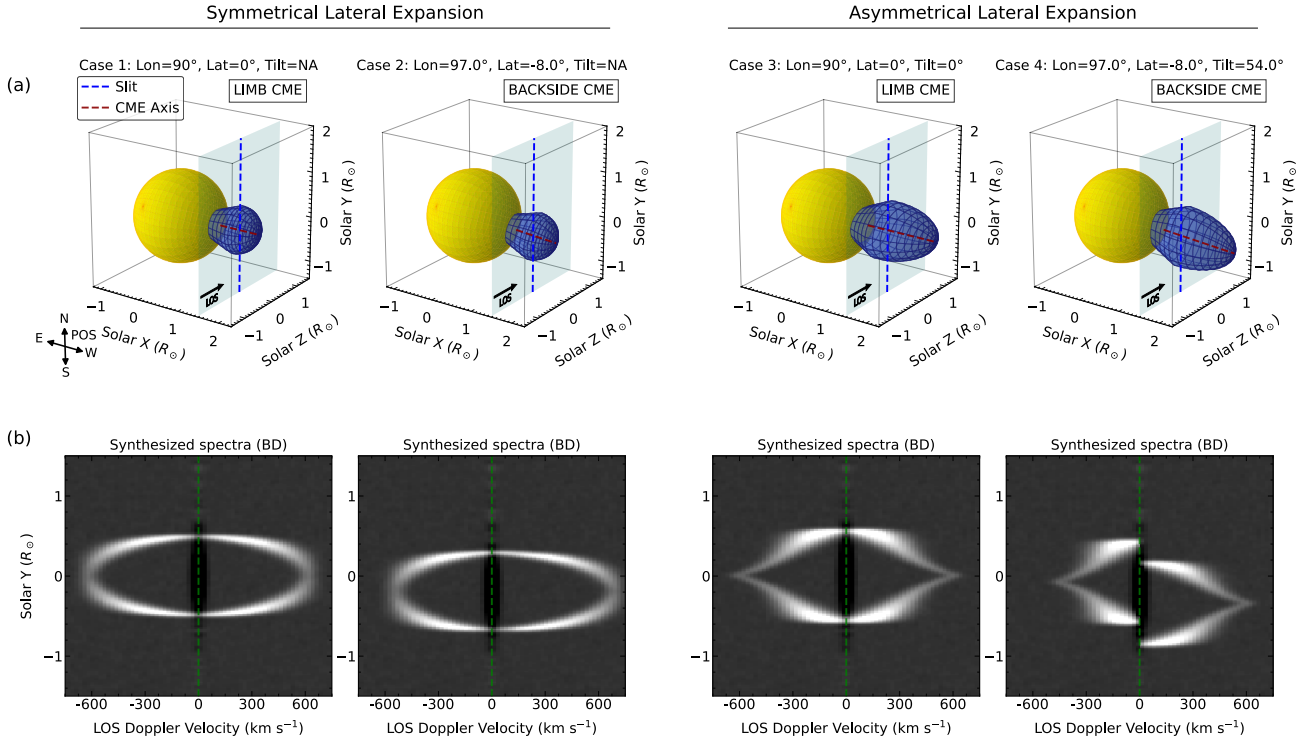


Figure 5. Three-dimensional modeling of the CME geometry and synthesized spectra for four model configurations. The upper panels (a) show the CME geometry, with the yellow sphere representing the Sun and the blue structure representing the CME. The red dashed lines indicate the CME axis. The line-of-sight (LOS) emission-integration plane is highlighted by the shaded plane, which also shows the slit orientation marked in blue. Cases 1 and 2 assume symmetric lateral expansion, while Cases 3 and 4 include asymmetric lateral expansion. Cases 1 and 3 represent a limb CME, whereas Cases 2 and 4 represent a backside CME with the GCS-derived CME orientation. The GCS-derived orientation corresponds to a CME located 7° behind the solar limb, is referred to as the "Backside CME" configuration. The lower panels (b) show the synthesized base-difference (BD) spectral maps along the slit, as a function of LOS Doppler velocity and projected Solar *Y* position. The LOS Doppler velocity and intensity in the synthetic spectra are shown in arbitrary scales. The results illustrate how CME orientation, axis tilt and lateral expansion modify the spatial and spectral morphology of the emission. An animation of this figure showing the synthetic spectral evolution for all four configurations is available online.

(An animation of this figure is available in the online article.)

spectral evolution for all four configurations. Among them, Case 4 also shows a spatiotemporal evolution of the bifurcated spectral structure that closely resembles the VELC observations. Thus, the observed spectral morphology and its evolution are consistent with an inclined axially tilted CME undergoing nonuniform lateral expansion.

4. Discussion

The AIA and VELC observations provide complementary constraints on the CME evolution in the low corona. AIA 211 Å traces the projected propagation of the CME front and the associated coronal dimming, while VELC spectroscopy reveals the Doppler-shifted plasma motions as the CME crosses Slit S4. The combination therefore provides information on both the POS propagation and the LOS velocity structure of the expanding CME.

During the CME passage, the VELC Fe XIV profiles develop distinct red- and blueshifted components at different locations along Slit S4. Their spatial separation indicates that different portions of the erupting structure contribute to the observed Doppler emission, revealing multiple velocity components within the expanding CME. The finite spectral range limits the LOS velocity measurement: the Doppler-shifted secondary component reaches the edge of the available spectral window, so its fitted centroid, corresponding to a Doppler shift of $+217.9\,\mathrm{km\,s^{-1}}$ is likely a lower limit to the LOS velocity of the receding plasma. Despite this limitation, the distinct bifurcated spectral shape and its spatiotemporal evolution provide important information on the LOS component of the CME lateral expansion.

The combined AIA and VELC observations show that the CME evolves nonuniformly in the low corona. The projected radial propagation speed of the CME front is $1134.9\,\mathrm{km\,s^{-1}}$, compared with a projected POS propagation speed of $691.5\,\mathrm{km\,s^{-1}}$ along Slit S4. This difference indicates that the CME expansion is not uniform in different directions, consistent with previous observations of anisotropic and nonself-similar CME expansion in the low corona (H. Cremades et al. 2020; S. Majumdar et al. 2020).

The Doppler-selected red-wing features propagate across the slit at $\sim$602–462 $\mathrm{km\,s^{-1}}$, with the projected propagation speed decreasing as the redshifted velocity increases. This trend does not necessarily imply that plasma with a larger LOS velocity is intrinsically slower. Rather, the Doppler-selected features can sample different parts of the expanding CME shell, where the velocity vector has different projections onto the LOS and POS. Plasma near the POS-lateral front of the expanding shell, as sampled along the slit, has a larger POS component and a smaller LOS component, whereas plasma closer to the center of the expanding structure has a larger LOS component and a smaller projected POS component. The

velocity-dependent propagation therefore indicates a change in the direction of the velocity vector across the expanding CME.

The three-dimensional model provides a geometric interpretation of the observed spectral structure. A model with symmetric lateral expansion does not reproduce the observed spectral morphology as closely as a model with different expansion rates along two perpendicular directions. The CME orientation affects the LOS contribution from the radial and axis tilt affects lateral motions and the displacement of the red- and blueshifted components, while asymmetric lateral expansion changes their spatial and spectral extent. The combination of the observed CME orientation, axis tilt, and asymmetric lateral expansion produces a spectral structure similar to that observed by VELC. The accompanying animation shows the synthetic spectral evolution for all four model configurations. Case 4, which combines the observed CME orientation (GCS-derived) with asymmetric lateral expansion, produces a bifurcated spectral morphology that shows a close visual resemblance to the VELC observations in both spatial structure and temporal evolution.

Note that the lower branch of the observed bifurcated spectral structure is relatively faint and cannot be clearly distinguished throughout the event because of its low signal-to-noise ratio. However, a closer inspection of the animation (Figure 2) reveals faint signatures of this lower branch and suggests an asymmetric spectral extent, with the right branches extending farther than the left. The two Doppler-shifted branches on the right also appear slightly displaced toward lower heights relative to their counterparts on the left. These features show a close visual resemblance to the spectral evolution produced by Case 4. Furthermore, the comparison is limited by the finite spectral range of the VELC observations. The LOS velocity in Figure 5(b) is shown on an arbitrary scale, with synthetic spectra extended to $\sim\pm750\,\mathrm{km\,s^{-1}}$, to illustrate the bifurcated spectral structure over a broader velocity range than VELC observes ($\sim\pm235\,\mathrm{km\,s^{-1}}$; Figure 2(c)). The pointed features at the edges of the synthetic spectra therefore likely reflect emission that VELC does not detect in the late evolution phase. Nevertheless, the model spectra and the observed spectral evolution show close agreement in their spatiotemporal evolution within the inner spectral range.

One possible explanation for the nonuniform lateral expansion is an asymmetric magnetic environment around the erupting CME. The expanding structure is confined by the magnetic pressure and tension of the surrounding corona, and an imbalance in these forces can allow greater expansion toward regions of weaker magnetic confinement. Such an asymmetric magnetic environment has been suggested as a possible cause of nonuniform CME expansion (P. F. Chen 2011). Recent observations also show lateral deformation of CME structures associated with their interaction with the surrounding magnetic field (H. Hu et al. 2026). The asymmetric expansion inferred in this event may therefore be related to nonuniform magnetic confinement in the surrounding corona, although the present observations do not provide sufficient constraints to establish this connection.

5. Summary

We investigated the early evolution of a fast CME observed on 2024 August 5 using Fe XIV 5303 Å spectroscopy from VELC together with AIA observations. AIA provides the projected radial and lateral propagation speeds in the POS, while VELC provides the LOS velocity structure of the expanding plasma. The VELC spectra reveal Doppler-shifted emission associated with the CME leading edge, with oppositely directed LOS motions producing a bifurcated spectral structure. The Doppler-resolved propagation and spatial variation of the spectral components indicate that the velocity direction changes across the expanding CME. Although the Doppler-shifted component reaches the edge of the available spectral range and its maximum LOS velocity is likely not captured, its spectral shape and spatial evolution provide information on the LOS component of the CME lateral expansion. A three-dimensional model shows that an inclined CME with axis tilt and asymmetric lateral expansion can produce a spectral structure similar to that observed. Together, the observations and modeling support a picture of nonuniform three-dimensional CME expansion, with different radial, POS-lateral, and LOS-lateral velocity components.

Acknowledgments

We acknowledge the VELC payload team at the Indian Institute of Astrophysics (IIA) and ISRO for the successful development, operation of the ADITYA-L1 mission, and for providing the data. Aditya-L1 is an observatory class mission that is fully funded and operated by the Indian Space Research Organization (ISRO). The mission was conceived and realized with the help from various ISRO centers. The science payloads and science ready data products are realized by the payload PI institutes in close collaboration with ISRO centers. The PI institutes are: Indian Institute of Astrophysics (IIA); Inter University Centre for Astronomy and Astrophysics (IUCAA); Laboratory for Electro-optics Systems (LEOS/URSC); Physical Research Laboratory (PRL); U R Rao Satellite Centre (URSC); and Space Physics Laboratory (SPL/VSSC). We acknowledge the use of data from the Aditya-L1 mission of the Indian Space Research Organisation (ISRO), archived at the Indian Space Science Data Centre (ISSDC). We also acknowledge the use of extreme-ultraviolet imaging data from the Solar Dynamics Observatory (SDO), courtesy of NASA and the AIA science team. The SOHO/LASCO data used in this study are produced by a consortium of the Naval Research Laboratory (USA), Max-Planck-Institut für Sonnensystemforschung (Germany), Laboratoire d'Astrophysique de Marseille (France), and the University of Birmingham (UK); SOHO is a project of international cooperation between ESA and NASA.

Appendix A
Three-dimensional CME Model and Synthetic Spectra

We use a parameterized three-dimensional kinematic model to examine how the geometry and velocity field of an expanding CME produce the observed Doppler-shifted spectral structure. The model is intended for a qualitative comparison with the VELC observations and is not used to derive the three-dimensional geometry or velocity field of the observed CME. The adopted parameters are therefore representative.

A.1. CME Geometry

The CME is represented by a shell-like structure consisting of a conical section capped by a hemisphere, as illustrated in Figure A1. The tip of the conical section is anchored at the

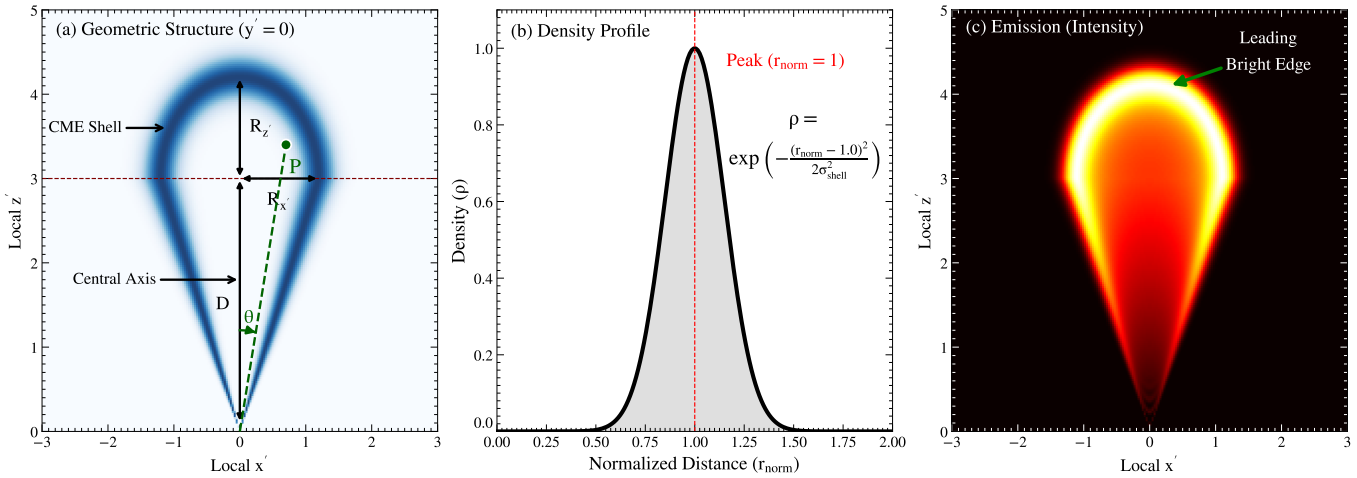


Figure A1. Geometry and density distribution of the CME model and the corresponding synthetic emission. Panel (a) illustrates the three-dimensional cone–hemispherical cross section at $y' = 0$, parameterized by the conical leg height (D), lateral thickness ($R_{x'}$), apex cap height ($R_{z'}$), and shell angle (θ) measured from the cone origin relative to the central axis for a shell point P. Panel (b) shows the density profile $\rho(r_{\rm norm})$ of CME shell as a function of the normalized distance $r_{\rm norm}$ from the central axis, with $r_{\rm norm} = 1$ representing position of density peak. Panel (c) shows the synthetic emission integrated along the y' direction.

center of the Sun, and the uppermost point of the hemispherical cap defines the CME apex. The modeled structure consists of a high-density shell with finite thickness and a relatively low-density interior. The density is assumed to peak at a reference surface and to decrease away from this surface following a Gaussian profile. Thus, most of the emission originates from a finite-thickness shell.

We introduce a local Cartesian coordinate system (x', y', z') attached to the CME. The origin is located at the vertex of the cone, and the $+z'$-axis is directed along the radial propagation direction toward the CME apex. A point on the CME surface is specified by the shell angle θ measured from the $+z'$-axis and the azimuthal angle ω around the z'-axis. The shell angle varies from $\theta = 0°$ at the apex to $|\theta| < 90°$ toward the lateral flanks.

A.2. Velocity Field

The CME velocity field consists of radial propagation and lateral expansion. The radial velocity, $v_{\rm rad}$, is directed along the CME propagation axis, while the lateral velocity, $v_{\rm lat}$, is perpendicular to this axis. The radial component dominates near the apex, whereas lateral expansion becomes increasingly important toward the flanks. We describe the transition between these two components as

$$v(\theta, \omega) = v_{\rm lat}(\omega) + [v_{\rm rad} - v_{\rm lat}(\omega)]e^{-A|\theta|}, \quad \text{(A1)}$$

where A controls the transition from radial propagation near the apex to lateral expansion toward the flanks.

To allow for asymmetric lateral expansion, the lateral velocity is specified by two orthogonal components, $v_{{\rm lat},x'}$ and $v_{{\rm lat},y'}$. The effective lateral expansion velocity at azimuth ω is

$$v_{\rm lat}(\omega) = \frac{v_{{\rm lat},x'} v_{{\rm lat},y'}}{\sqrt{(v_{{\rm lat},y'}\cos\omega)^2 + (v_{{\rm lat},x'}\sin\omega)^2}}. \quad \text{(A2)}$$

For $v_{{\rm lat},x'} = v_{{\rm lat},y'}$, the lateral expansion is symmetric. Unequal values produce an elliptical cross section and asymmetric expansion. The velocity components in the local CME coordinate system are then

$$v'_x = v(\theta, \omega)\sin\theta\cos\omega, \quad \text{(A3)}$$

$$v'_y = v(\theta, \omega)\sin\theta\sin\omega, \quad \text{(A4)}$$

$$v'_z = v(\theta, \omega)\cos\theta. \quad \text{(A5)}$$

A.3. CME Orientation

The local CME coordinate system is transformed to a heliocentric Cartesian coordinate system (X, Y, Z), where the Z-axis is directed along the observer's LOS and the XY-plane defines the POS. The position of the CME on the solar surface is specified by its heliographic longitude ϕ and latitude λ. These angles determine the orientation of the CME propagation axis with respect to the observer.

An additional tilt angle γ describes the rotation of the CME cross section about the propagation axis. This parameter is relevant only when the cross-section is elliptical, as arises in our model due to nonuniform lateral expansion. The resulting transformation determines the orientation of the CME with respect to the plane of the sky and the line of sight. For the configurations representing the observed CME, we adopt $\phi = 97°$, $\lambda = -8°$, and $\gamma = 54°$, based on the GCS reconstruction described in Appendix B.

A.4. Synthetic Fe XIV Spectra

To compare the model with the VELC observations, we synthesize the Fe XIV 5303 Å emission from the model CME. The calculation includes only the prescribed geometry, density distribution, and velocity field. We do not model the thermodynamic evolution, ionization state, or detailed excitation conditions of the CME. Instead, we assume optically thin emission produced by collisional excitation and use the model density to prescribe the relative emissivity.

The synthetic spectral intensity at a position (X, Y) is obtained by integrating the emission along the line of sight,

$$I(X, Y, \nu) = \int \epsilon(X, Y, Z)\, \mathcal{G}[\nu - V_{\rm LOS}(X, Y, Z)]\, dZ, \quad \text{(A6)}$$

where ν is the Doppler velocity used as the spectral coordinate, $V_{\rm LOS}$ is the local LOS velocity, and ϵ is the local emissivity. We assume

$$\epsilon \propto n^2, \quad \text{(A7)}$$

where n is the model density. The function $\mathscr{G}$ represents a Gaussian local emission profile centered at the local LOS velocity. The intrinsic width is assumed to be constant throughout the CME.

Because the density is concentrated in the shell, the synthesized emission is dominated by regions where the line of sight intersects the CME shell. The resulting spectra therefore depend on both the orientation of the shell and the LOS component of its velocity field.

For comparison with the observations, synthetic spectra at the initial time are subtracted from those at subsequent times to produce base-difference (BD) spectra. For constructing synthetic BD spectra, the initial state is taken as the preeruption reference state and have no CME-associated bulk motion.

A.5. Model Configurations

We consider four representative configurations to separate the effects of CME orientation and asymmetric lateral expansion. The corresponding geometries and synthesized base-difference spectra are shown in Figure 5.

The first configuration represents a CME at the solar limb with symmetric lateral expansion. The front and rear portions of the expanding shell produce oppositely directed LOS velocities. The resulting red- and blueshifted components form an approximately symmetric, semicircular pattern. The LOS velocity is largest near the center of the CME, where the lateral expansion has its largest LOS projection, and decreases toward the upper and lower boundaries where the expansion becomes increasingly perpendicular to the LOS.

The second configuration uses the heliographic location obtained from the GCS reconstruction while retaining symmetric lateral expansion. The CME is located behind the limb and propagates partly away from the observer, introducing an additional LOS component from the radial propagation. As a result, the red- and blueshifted components have different Doppler amplitudes. .

The third configuration has the same limb location as the first case, and without any axis tilt, but introduces asymmetric lateral expansion. The lateral expansion speed along the LOS is larger than that along the Solar Y direction. Consequently, the LOS velocity decreases more rapidly away from the center of the CME, changing the spectral morphology from the semicircular pattern of Case 1 to a more pointed structure.

The fourth configuration combines the GCS-constrained CME orientation and tilt with the asymmetric lateral expansion of Case 3. It therefore retains the Doppler asymmetry and displacement produced by the CME axis tilt while producing the pointed spectral morphology associated with asymmetric lateral expansion. Among the four configurations, Case 4 shows the closest qualitative correspondence with the VELC observations, both in the spectral morphology and its temporal evolution.

These configurations are intended to isolate the geometric effects that influence the synthetic spectra. They are not a parameter search or a quantitative inversion of the observed CME geometry or velocity field. A quantitative inversion framework will be developed in future work to constrain the three-dimensional CME geometry and velocity field from spectroscopic observations.

Appendix B
GCS Fitting

We used the GCS model (A. F. R. Thernisien et al. 2006; A. Thernisien et al. 2009; A. Thernisien 2011) to estimate the propagation direction and axis orientation of the CME. The reconstruction was performed using multiviewpoint coronagraph observations from SOHO/LASCO and STEREO/COR, together with the available EUV observations (Figure B1). The GCS wireframe was adjusted to the observed CME morphology in the different viewpoints.

The best-fit configuration gives a CME longitude of 97°, latitude of −8°, and an axis tilt of 54°. These parameters are used in our three-dimensional CME model to set the CME orientation with respect to the observer. They are not adjusted during the spectral modeling and are not used to derive the CME velocity field. The GCS reconstruction therefore, provides the orientation constraint for the model, while the lateral expansion parameters are varied independently.

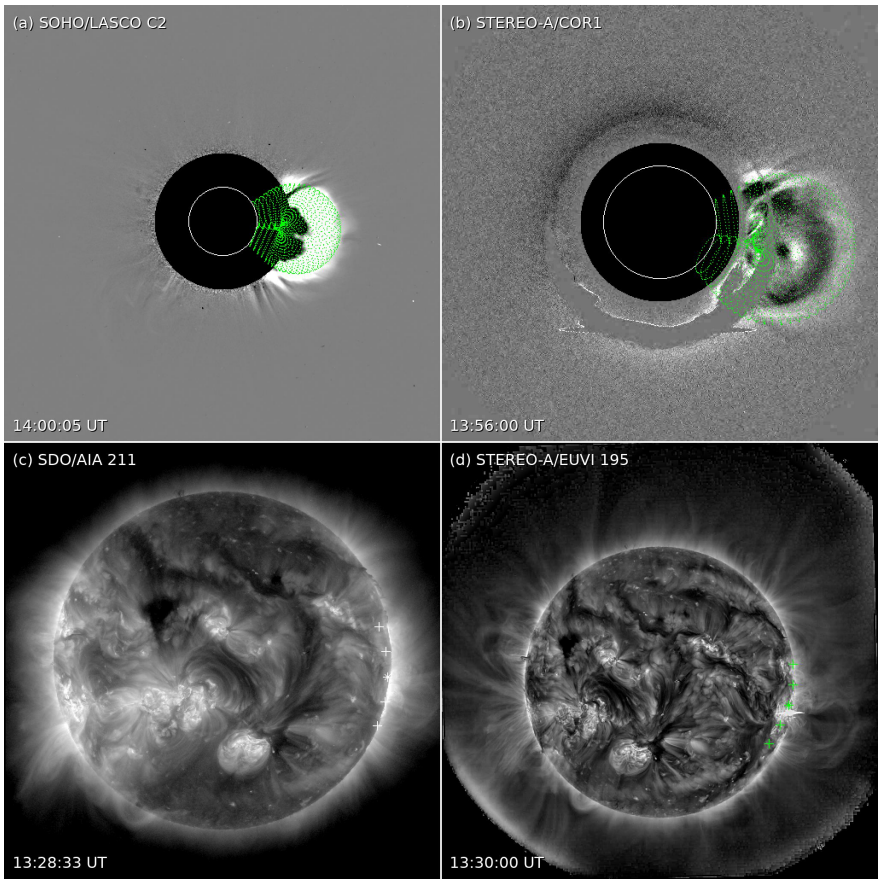


Figure B1. GCS reconstruction of the 2024 August 5 CME using multiviewpoint coronagraph and EUV observations. The best-fit GCS wireframe (green mesh) is overlaid on the observed CME in the coronagraph panels. The reconstruction gives a CME longitude of 97°, latitude of −8°, and an axis tilt of 54°. The green "+" symbols in the lower panels mark the corresponding footpoint locations. These GCS-derived parameters are used to set the CME orientation in our three-dimensional CME model.

ORCID iDs

Saurabh Tripathi https://orcid.org/0009-0006-7404-4235
Tanmoy Samanta https://orcid.org/0000-0002-9667-6392
Jayant Joshi https://orcid.org/0000-0003-0585-7030

References

Agarwal, A., Mishra, W., Zhang, J., Khuntia, S., & Temmer, M. 2026, ApJ, 1008, 137
Brueckner, G. E., Howard, R. A., Koomen, M. J., et al. 1995, SoPh, 162, 357
Chan, L., Bai, X., Tian, H., et al. 2025, ApJ, 984, 141
Chen, J. 2017, PhPl, 24, 090501
Chen, P. F. 2011, LRSP, 8, 1
Cheng, X., Zhang, J., Olmedo, O., et al. 2012, ApJL, 745, L5
Cremades, H., Iglesias, F. A., & Merenda, L. A. 2020, A&A, 635, A100
Culhane, J. L., Harra, L. K., James, A. M., et al. 2007, SoPh, 243, 19
Frassati, F., Mancuso, S., & Bemporad, A. 2020, SoPh, 295, 124
Georgoulis, M. K., Nindos, A., & Zhang, H. 2019, RSPTA, 377, 20180094
Gopalswamy, N. 2004, ASSL, 317, 201
Gopalswamy, N., & Hanaoka, Y. 1998, ApJL, 498, L179
Gosling, J. T., Bame, S. J., McComas, D. J., & Phillips, J. L. 1990, GeoRL, 17, 901
Howard, R. A., Moses, J. D., Vourlidas, A., et al. 2008, SSRv, 136, 67
Howard, R. A., Vourlidas, A., & Stenborg, G. 2023, FrASS, 10, 2023
Hu, H., Chen, C., Jiao, Y., et al. 2026, ApJ, 997, 303
Kohl, J. L., Esser, R., Gardner, L. D., et al. 1995, SoPh, 162, 313
Kozarev, K. A., Davey, A., Kendrick, A., Hammer, M., & Keith, C. 2017, JSWSC, 7, A32
Kozarev, K. A., Korreck, K. E., Lobzin, V. V., Weber, M. A., & Schwadron, N. A. 2011, ApJL, 733, L25
Landi, E., Raymond, J. C., Miralles, M. P., & Hara, H. 2010, ApJ, 711, 75
Lemen, J.R., Title, A. M., Akin, D. J., et al. 2012, SoPh, 275, 17
Liu, W., & Ofman, L. 2014, SoPh, 289, 3233
Liu, W., Ofman, L., Nitta, N. V., et al. 2012, ApJ, 753, 52
Liu, X., Tian, H., Török, T., et al. 2023, SoPh, 298, 112
Ma, S., Raymond, J. C., Golub, L., et al. 2011, ApJ, 738, 160
Majumdar, S., Pant, V., Patel, R., & Banerjee, D. 2020, ApJ, 899, 6
McIntosh, S. W., De Pontieu, B., & Leamon, R. J. 2010, SoPh, 265, 5
Muthu Priyal, V., Ramesh, R., Singh, J., & Sasikumar Raja, K. 2025, ApJ, 983, 171
Patsourakos, S., & Vourlidas, A. 2012, SoPh, 281, 187
Patsourakos, S., Vourlidas, A., & Stenborg, G. 2010, ApJL, 724, L188
Priyal, M., Singh, J., Prasad, B. R., et al. 2024, AdSpR, 74, 547
Priyal, V. M., Ramesh, R., Singh, J., Sasikumar Raja, K., & Gopalswamy, N. 2025, ApJ, 994, 182
Ramesh, R., Muthu Priyal, V., Singh, J., et al. 2024, ApJL, 976, L6
Raymond, J. C., Ciaravella, A., Dobrzycka, D., et al. 2003, ApJ, 597, 1106
Raymond, J. C., Thompson, B. J., St. Cyr, O. C., et al. 2000, GeoRL, 27, 1439
Shibata, K., & Magara, T. 2011, LRSP, 8, 6
Singh, J., Prasad, B. R., Venkata, S., & Kumar, A. 2019, AdSpR, 64, 1455
Singh, J., Ramesh, R., Prasad, B. R., et al. 2025, SoPh, 300, 66
Thernisien, A. 2011, ApJS, 194, 33
Thernisien, A., Vourlidas, A., & Howard, R. A. 2009, SoPh, 256, 111
Thernisien, A. F. R., Howard, R. A., & Vourlidas, A. 2006, ApJ, 652, 763
Tian, H., McIntosh, S. W., Xia, L., He, J., & Wang, X. 2012, ApJ, 748, 106
Tian, H., Tomczyk, S., McIntosh, S. W., et al. 2013, SoPh, 288, 637
Veronig, A. M., Dissauer, K., Kliem, B., et al. 2025, LRSP, 22, 2
Vourlidas, A. 2021, FrASS, 8, 2021
Warmuth, A. 2015, LRSP, 12, 3
Webb, D. F., & Howard, T. A. 2012, LRSP, 9, 3
Wraback, E. M., Landi, E., Manchester, W. B., & Szente, J. 2025, ApJ, 980, 30
Zarro, D. M., Sterling, A. C., Thompson, B. J., Hudson, H. S., & Nitta, N. 1999, ApJL, 520, L139